Metastable Cu(I)-Niobate Semiconductor with a Low-Temperature, Nanoparticle-Mediated Synthesis

Jonglak Choi, Nacole King, and Paul A. Maggard*

Department of Chemistry, North Carolina State University, Raleigh, North Carolina 27695-8204, United States

ABSTRACT A nanoparticle synthetic strategy for the preparation of a new metastable Cu(I)-niobate is described, and that involves multipored Li_3NbO_4 nanoparticles as a precursor. A hydrothermal reaction of $HNbO_3$ and $LiOH \cdot H_2O$ in PEG200 and water at ~180 °C yields ~15−40 nm Li_3NbO_4 particles. These particles are subsequently used in a solvothermal copper(I)-exchange reaction with excess CuCl at 150 °C. Heating these products within the used CuCl flux (mp = 430 °C) to 450 °C for 30 min yields ~4−12 nm $Cu_2Nb_8O_{21}$ crystalline nanoparticles, and for a heating time of 24 h yields μm-sized, rod-shaped crystals. The new structure was characterized by single-crystal X-ray diffraction to have a condensed network consisting of NbO_7 polyhedra and chains of elongated CuO_4 tetrahedra. The compound thermally decomposes starting at ~250 °C and higher temperatures, depending on the particle sizes, owing to the loss of the weakly coordinated Cu(I) cations from the structure and a concurrent disproportionation reaction at its surfaces. Thus, conventional solid-state reactions involving higher temperatures and bulk reagents have proven unsatisfactory for its synthesis. The measured bandgap size is ~1.43−1.65 eV (indirect) and shows a dependence on the particle sizes. Electronic structure calculations based on density functional theory show that the bandgap transition results from the excitation of electrons at the band edges between filled Cu(I) $3d^{10}$-orbitals and empty Nb(V) $4d^0$-orbitals, respectively. The *p*-type nature of the $Cu_2Nb_8O_{21}$ particles was confirmed in photoelectrochemical measurements on polycrystalline films that show a strong photocathodic current under visible-light irradiation in aqueous solutions. These results demonstrate the general utility of reactive nanoscale precursors in the synthetic discovery of new Cu(I)-based semiconducting oxides and which also show promise for use in solar energy conversion applications.

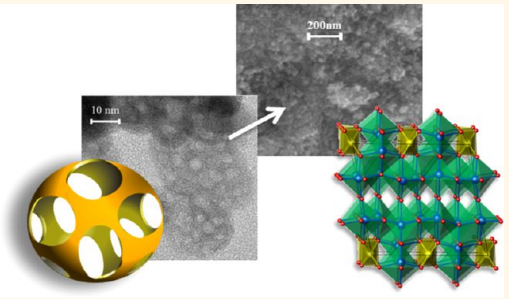

KEYWORDS: nanoscale synthesis · solar energy · metastability · copper niobate · lithium niobate

The discovery of new materials for use in solar-energy conversion schemes has received intense research interest as a promising way to increase their efficiency.[1,2] As nearly half of the incident solar energy on the Earth's surface falls in the visible-light energy range, new semiconductors are sought with bandgap sizes that more closely match this lower-energy component of the solar spectrum. Recently, our research approach has focused on semiconducting oxides that contain M/M' transition-metal combinations (e.g., *M* = Cu(I); *M'* = Ta(V) or Nb(V)) that exhibit visible-light bandgap sizes owing to low-energy, metal-to-metal charge transfer transitions between crystal orbitals originating from the filled d^{10} and empty d^0 electronic configurations, respectively.[3] For example, $CuNbO_3$,[4] $CuNb_3O_8$,[5] $Cu_5Ta_{11}O_{30}$, and $Cu_3Ta_7O_{19}$[6,7] all show bandgap sizes with visible-light energies, spanning values between ~1.3 to 2.6 eV. Their conduction bands also typically maintain a suitably negative redox potential with respect to the fuel-producing redox reactions, such as the reduction of water to hydrogen. In solar-to-fuel energy conversion schemes, two of the most prominent strategies involve either their use as photocatalysts in the form of suspended powders in solution, or their use as photoelectrodes in a photoelectrochemical cell. The most efficient configurations of each of these applications require that the materials be prepared in a nanosized, high-surface-area format that can maximize the area of reactive surfaces and the efficiency of the charge-carrier collection.[8] Recent examples illustrating the advantages of nanoscale materials in solar-energy conversion

* Address correspondence to paul_maggard@ncsu.edu.

Received for review December 11, 2012 and accepted January 31, 2013.

Published online January 31, 2013
10.1021/nn305707f

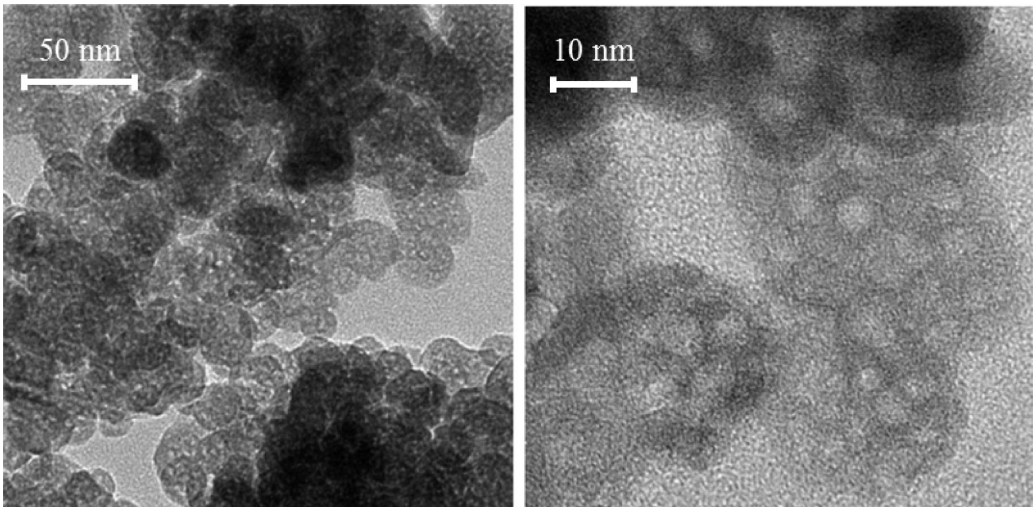

Figure 1. TEM images of multipored Li_3NbO_4 nanoparticles with diameters of ~15−40 nm.

schemes include nanostructured α-Fe_2O_3 photoanodes,[9] photocatalytic nanoparticles of $SrTiO_3$, and nanosheets of $KCa_2Nb_3O_{10}$,[10,11] as well as many others.[12−16]

A significant amount of literature has been reported on the synthesis of many types of nanosized metal-oxides, such as with ABO_3-perovskite or $A_2B_2O_7$-pyrochlore types of structures (A = alkali metal; B = transition metal).[17] A careful selection of the reaction conditions (e.g., solvent, pH, temperature, time, capping agents, *etc.*) has demonstrated a variety of possible nanoparticle morphologies, such as nanoribbons, nanoflowers, and nanocubes, that can be grown ranging from ~10 nm to >~200 nm in size. These nanoparticles are promising for the creation of nanotextured polycrystalline films with controllable surface areas, crystal facets, and film porosities. However, with the exception of simple Cu_2O, the nanoparticle synthesis of mixed-metal oxides containing Cu(I) has remained limited because of the inherent instability of the Cu(I) oxidation state. Both high temperatures as well as exposure to air and water must be carefully avoided in their nanoparticle synthesis. The lithium-containing metal oxides, including Li_3MO_4, LiM_3O_8, and $LiMO_3$ (M = Ta(V) and Nb(V)),[18−21] have been shown to represent promising reactive precursors to prepare new mixed-metal oxides. Several of these are known to exhibit a high Li-ion mobility, are highly reactive, and can frequently be converted *via* ion-exchange reactions to other types of metal oxides.[22] Recent investigations show that both $LiNbO_3$ and Li_3NbO_4 can be relatively easily prepared by solvothermal methods in nanoparticle form.[18,19] Thus, the synthesis of lithium-niobate nanoparticles for use as highly reactive precursors represents a very promising soft chemical pathway to produce new mixed-metal oxides, especially for those that might not be stable under more conventional solid-state synthesis conditions.

Described herein is the solvothermal synthesis of multipored Li_3NbO_4 nanoparticles and their reaction with CuCl at relatively low temperatures to prepare nanoparticles of the new metastable $Cu_2Nb_8O_{21}$ semiconductor. These nanoparticles grow rapidly in the CuCl flux to produce large single crystals that were structurally characterized by X-ray diffraction. The particles were also characterized by electron microscopy techniques and their thermal instability was investigated by powder X-ray diffraction. Optical and photoelectrochemical properties measurements on the $Cu_2Nb_8O_{21}$ particles were used to characterize their visible-light bandgap sizes and their *p*-type nature in the form of polycrystalline films. Electronic structure calculations were also utilized to understand the origins and size of their bandgap transitions.

RESULTS AND DISCUSSION

Synthesis. *Precursor Li_3NbO_4 Nanoparticles.* As the synthesis of Cu(I)-based mixed-oxide nanoparticles has been found to be unstable toward disproportionation or oxidation during many attempted reactions, a new highly reactive and high-surface-area precursor was found to be necessary for their preparation. The Li_3NbO_4 phase has a high Li-ion mobility, and thus its nanoparticle synthesis was investigated as a potentially promising route to Cu(I)-niobate nanoparticles. As shown in the TEM data in Figure 1, the prepared Li_3NbO_4 nanoparticles (~15−40 nm in diameter; histogram in Figure S8) have roughly spherical morphologies with multiple internal pores. The product also exhibits a high purity, as confirmed by PXRD (Supporting Information, Figure S1), with a measured specific surface area of ~45 m^2/g. The formation of microemulsions within a polyethylene glycol/water mixture is generally understood to be responsible for the crystallization of these multipored particles, such as previously reported for the μm-sized hollow particles of $LiNbO_3$.[23] In nondilute

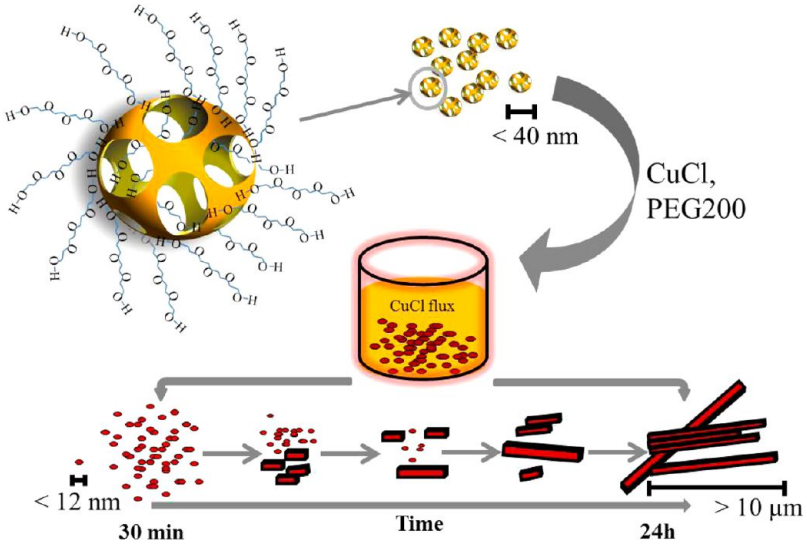

Scheme 1. Synthetic Transformation of Hollow Li_3NbO_4 Nanoparticles to $Cu_2Nb_8O_{21}$ Nanoparticles, Followed by Their Further Growth into Micrometer-Sized Single Crystals

solutions, the possible types of self-assembled colloidal structures are a sensitive function of the reaction conditions. Reactions performed using lower amounts of polyethylene glycol (PEG200) produced larger nanoparticles with a specific surface area of ~17 m^2/g, and higher amounts of it produced mixed lithium-niobate phases. The solubility of LiOH in the solution was found to have a significant influence on the particle sizes and product distribution.

The overall reactivity and instability of these Li_3NbO_4 nanoparticles was found to be more enhanced compared to other reported preparations and to other lithium-niobate phases. In aqueous solutions these nanoparticles lose Li cations continuously, with each washing resulting in a slight shifting of the PXRD peaks. Other preparations of Li_3NbO_4 are stable in air at up to ~700 °C,[24] but these multipored nanoparticles decompose in air by 400 °C to a mixture of $LiNbO_3$ and $LiNb_3O_8$, Figure S1. A flame test on the solution from the washed product confirmed the low-temperature loss of Li cations from the Li_3NbO_4 nanoparticles. Also, the Li_3NbO_4 nanoparticles decompose immediately within *c*-HCl to an amorphous hydrated niobate, and which crystallizes as Nb_2O_5 upon heating to 450 °C for 12 h.

Cu(I)-Niobate Nanoparticles. Lower temperatures, as well as the absence of air and moisture, were found to be necessary in the ion-exchange solvothermal reaction of CuCl with the Li_3NbO_4 nanoparticles. To the best of our knowledge the synthesis of Cu(I)-based mixed-oxide nanoparticles, specifically with early transition-metal oxides, has not previously been reported. Illustrated in Scheme 1 is the overall reaction strategy that was used. As shown in the PXRD data and SEM images in Figures 2 and 3, respectively, these reactions yielded crystalline $Cu_2Nb_8O_{21}$ nanoparticles that grew rapidly into μm-sized single crystals during a heating

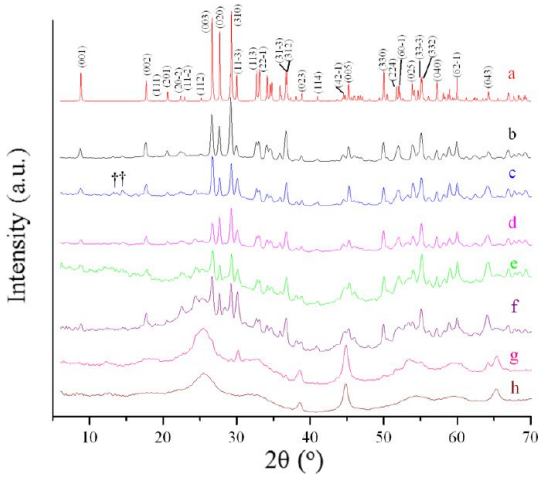

Figure 2. PXRD plots of simulated $Cu_2Nb_8O_{21}$ from the (a) single crystal data, and products heated to 450 °C for (b) 1 day, (c) 8 h, (d) 5 h, (e) 1 h, (f) 30 min using 7 °C/m ramping rate, (g) 30 min using 15 °C/m ramping rate, and (h) heated at 400 °C for 30 min. Note: + = peak from capillary quartz tube for XRD, † = unidentified peaks.

duration of between 30 min to 24 h. The measured surface areas of each of the products are listed in Table 1. The calculated PXRD of $Cu_2Nb_8O_{21}$ in Figure 2 was determined from the structural refinement of a single crystal obtained from a 24 h reaction at 650 °C, described below. For a heating time of 1 h, the PXRD data show the distinct emergence of diffraction peaks corresponding to the $Cu_2Nb_8O_{21}$ phase and which originate from a smaller set of broad diffraction peaks observed in the shorter heating duration of 30 min, Figure 2e,g. The surface areas decrease only slightly between the 30 min and 1 h heating times of ~43 to ~39 m^2/g, respectively. This transformation is also observable in the electron microscopy images in Figure 3, with the formation of distinct rod-like nanoparticles in

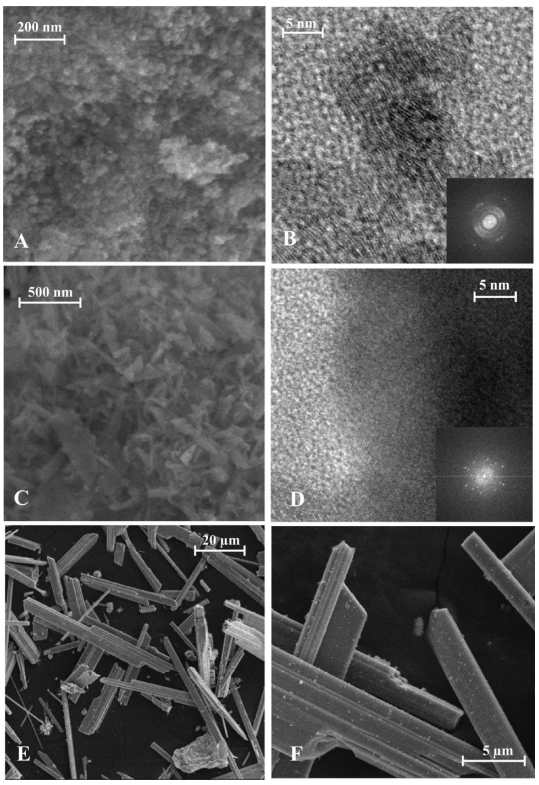

Figure 3. Electron microscopy images of $Cu_2Nb_8O_{21}$ after annealing at 450 °C for 30 min (A, B), 1 h (C, D), and 24 h (E, F). The insets in the TEM images of B and D show the selected area of electron diffraction patterns, while SEM images are shown in A and C.

TABLE 1. Surfaces Areas and Bandgap Sizes of $Cu_2Nb_8O_{21}$ Prepared *via* Different Reaction Times

heating duration[a]	24 h	8 h	5 h	1 h	30 min, ramped 7 °C/min	30 min, ramped 15 °C/min
surface area (m^2/g)	2.7	10	12	39	43	52
bandgap size (eV)	1.65	1.62	1.58	1.54	1.43	1.43

[a] All samples were heated to 450 °C in an evacuated fused-silica vessel for a duration of between 24 h and 30 min.

Figure 3c,d, compared to the more spherical nanoparticles in Figure 3a,b. The measured particle sizes from the TEM data vary from 4 to 12 nm for the 30 min reaction (histogram in Figure S8) and from 4 to 28 nm for the 1 h reaction. In comparing the SAED of each, Figure 3b,d, the extent of single-crystalline features is more prominent in the $Cu_2Nb_8O_{21}$ nanoparticles at 1 h. Simulation of the transmission electron diffraction can be approximately matched to the *d*-spacing present for the [101] zone axis (Supporting Information), consistent with a growth direction of the rod-like crystals down the *b*-axis. The longest growth duration of 24 h results in the formation of large single crystals, Figure 3e,f, and an intermediate growth duration results in a product mixture that contains both relatively smaller single crystals and nanoparticles (see Supporting Information), with a much smaller surface area of ~2.7 m^2/g. At lower temperatures of 400 °C, there is no growth of the $Cu_2Nb_8O_{21}$

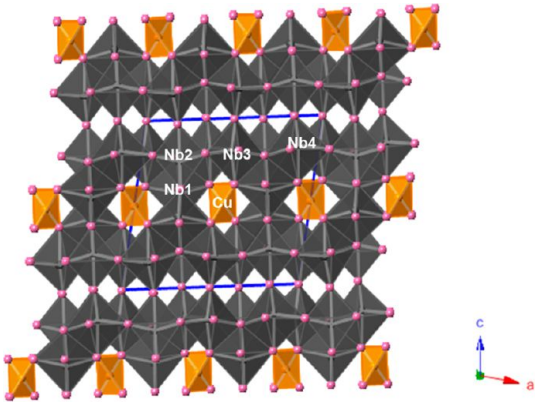

Figure 4. Polyhedral structural view of the overall unit cell of $Cu_2Nb_8O_{21}$. Selected atoms are labeled; oxygen atoms are pink, gray polyhedra are NbO_7, and orange polyhedra are CuO_4.

nanoparticles into single crystals, as CuCl melts at ~430 °C. Thus, the excess CuCl from the solvothermal products is critical for both the Li/Cu ion-exchange as well as in the subsequent rapid flux-assisted growth of the large single crystals.

The nanoparticle formation of other Cu(I)-niobates, for example, Li-doped $CuNb_3O_8$ and $CuNbO_3$, was also observed over the course of these synthetic investigations. The distribution and purity of the obtained Cu(I)-niobates are highly sensitive to the preparation conditions, including the temperature, reaction duration, the amount of CuCl, and stirred *versus* nonstirred reactions. The reaction duration and the amount of excess CuCl are two of the most important factors in obtaining a particular Cu(I)-niobate product in the synthesis. For example, if the molar ratio of CuCl-to-Li_3NbO_4 is lowered to 4:1, then the formation of only Cu(I)-richer phases is observed, such as nanoparticles of $Cu_xLi_{1-x}Nb_3O_8$ and $Cu_xLi_{1-x}NbO_3$ (see Supporting Information). These Cu(I)-richer phases are known to form solid solutions with the Cu(I) and Li cations disordered over the same atomic sites and which is detectable here as a significant shifting of the X-ray diffraction peaks. For the washed $Cu_2Nb_8O_{21}$ products, the electron microscopy EDS data were all very close to the ideal 1:4 Cu-to-Nb ratio in the formula, as determined by single-crystal X-ray diffraction. Thus, the full replacement of Li for Cu(I) in these solvothermal reactions, followed by the thermal growth process, yields the formation of the new $Cu_2Nb_8O_{21}$ phase. Further synthetic investigations are underway to obtain pure $CuNb_3O_8$ and $CuNbO_3$ nanoparticles and which will be reported in subsequent complete studies.

Structural Description. The single crystals of $Cu_2Nb_8O_{21}$ were structurally characterized by X-ray diffraction to crystallize in a monoclinic space group (*C*2/*m*) with a condensed three-dimensional structure, as shown in Figure 4. Within the structure there are four symmetry-inequivalent Nb sites, one Cu site, and eight

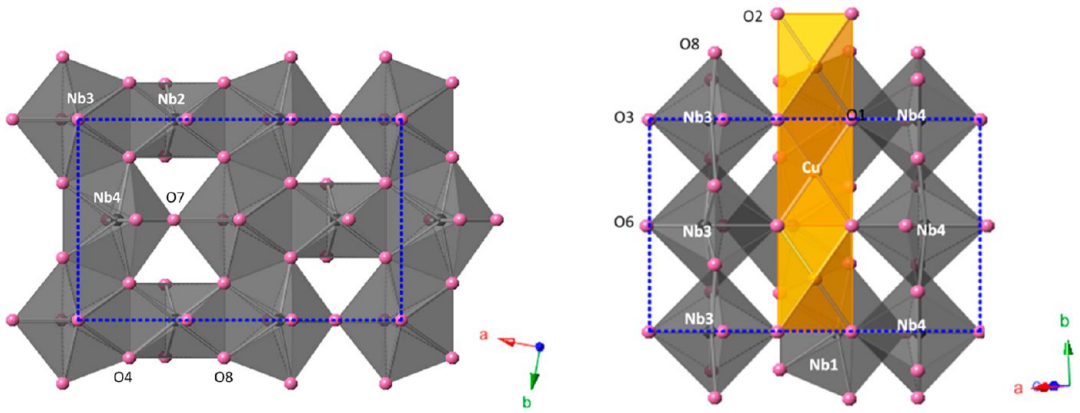

Figure 5. Polyhedral views, both perpendicular to the (110) plane, of a single niobate layer (left) and of the neighboring layer comprised of CuO_4/NbO_7 polyhedra (right). Selected atoms are labeled; oxygen atoms are pink, gray polyhedra are NbO_7, and orange polyhedra are CuO_4.

independent O sites, as listed in Table S2 with all nearest-neighbor distances. Generally, the structure consists of a double layer of distorted NbO_7 polyhedra that alternates with a layer of distorted CuO_4 tetrahedra and NbO_7 pentagonal bipyramids that form chains aligned down the [010] direction. These two types of layers are shown in Figure 5. The layer of NbO_7 polyhedra is constructed from edge-shared zigzag chains of the NbO_7 pentagonal bipyramids (Nb3−O and Nb4−O with distances of 1.765(2)Å to 2.229(3)Å). These zigzag niobate chains are condensed into a layer *via* both a corner-shared oxygen (O7), and also through an edge-shared NbO_7 monocapped trigonal prism (Nb2−O with distances of 1.988(2)Å to 2.185(2)Å). Two of these layers are condensed into a double layer *via* shared apical oxygen atoms (O3 and O6) of the NbO_7 pentagonal bipyramids, Figure S3. The double layers are in turn condensed to the layer of CuO_4 and NbO_7 chains through the opposing apical oxygen atoms on the NbO_7 pentagonal bipyramids (O1 and O2). Shown in Figure 5 (right), the distorted CuO_4 tetrahedra (Cu−O distance of 2.095(2) Å) are condensed into a chain *via* share edges and then further condensed to neighboring edge-shared chains of NbO_7 polyhedra to form a layer. These two types of layers, Figure 5 (left and right), thus form the full three-dimensional structure.

The $Cu_2Nb_8O_{21}$ phase is synthetically challenging to prepare, although all interatomic distances seemingly fall within reasonable values as reported before.[25,26] However, among the other known Cu(I)-niobates, that is, $CuNbO_3$, $CuNb_3O_8$, and $CuNb_{13}O_{33}$, their structures consist exclusively of distorted NbO_6 octahedra rather than the NbO_7 polyhedra observed in $Cu_2Nb_8O_{21}$. Conversely, the Cu(I)-tantalates, that is, $Cu_5Ta_{11}O_{30}$ and $Cu_3Ta_7O_{19}$, exhibit structures constructed from layers of TaO_7 pentagonal bipyramids. Within the pentagonal bipyramidal coordination environments, the greater covalent character of the Nb−O bonds (especially to the two apical oxygen atoms) compared to the Ta−O bonds causes longer bond distances to vertex-bridged Cu(I)−O interactions, that is, across the Nb−O−Cu bridges. This is a relationship that has been observed previously in the $NaCu(Ta_{1-y}Nb_y)_4O_{11}$ solid solution,[27] wherein the substitution of Ta for Nb causes a shortening of the apical M − O distances concomitant with a lengthening and weakening of the Cu−O interactions. Shown in Table S2 for $Cu_2Nb_8O_{21}$, the calculated bond valence sums[28,29] are higher than expected for Nb (+5.1 to +5.3) and lower than expected for Cu (+0.74), consistent with an overall relatively stronger coordination of Nb and a weaker coordination around Cu than typically observed within structures. The instability of $Cu_2Nb_8O_{21}$ results in a re-equilibration of these out-of-balance interactions, such as can happen from a structural rearrangement or from the removal of the weakly coordinated Cu(I) atoms from the compound, as described below.

Thermal Instability. While the synthesis of both $CuNbO_3$ and $CuNb_3O_8$ can be performed using conventional solid-state reactions between bulk Cu_2O and Nb_2O_5, numerous attempts at the bulk solid-state synthesis of $Cu_2Nb_8O_{21}$ have not been successful. Currently, the only alternate synthesis that has been found to work is the reaction of Cu_2O nanoparticles (~10−20 nm) with Nb_2O_5 nanoparticles in a CuCl flux at 650 °C, but which does not yield nanoparticles. A highly reactive nanoparticle precursor and the low-melting CuCl flux have both been found to be necessary to obtain $Cu_2Nb_8O_{21}$. The CuCl-flux and the nanoparticles serve to lower the activation energy of the reaction and can help lead to the formation of potentially new metastable phases. Thus, the thermal stability and decomposition of the $Cu_2Nb_8O_{21}$ products were investigated in order to understand why this compound can only be prepared under these conditions, and which can help inform whether other possible Cu(I)-based mixed-metal oxides might be discovered using this approach.

The reactivity and thermal stability of both the $Cu_2Nb_8O_{21}$ nanoparticles and the μm-sized crystals

were investigated by heating (either under N_2 or in air) at increasing temperatures from 200 to 1000 °C, in intervals of 50 to 100 °C. All products at each temperature were characterized by powder X-ray diffraction techniques. The final end products are given in the PXRD of Figure 6, while all data at each temperature can be found in the Supporting Information. Both the nano- and μm-sized particles exhibited similar final products, but which generally formed at lower temperatures for the nanoparticles. When heating the $Cu_2Nb_8O_{21}$ particles under flowing N_2, these showed the formation of Cu(s) starting at ~250 °C for nanoparticles, and at ~300 °C for micrometer-sized crystals, but which was significantly more extensive for the nanoparticles. The other decomposition products of the nanoparticles were Nb_2O_5 and $Nb_{12}O_{29}$ at 750 °C and higher temperatures, while the μm-sized particles decomposed to $CuNbO_3$ and $CuNb_3O_8$ as well. In the latter case, the Cu(I) ions have a much longer distance to travel to reach the surfaces of the μm-sized crystals, and thus, the Cu(I) cannot be completely removed and the more stable Cu(I)-niobates are formed in the products. At temperatures as low as ~300 °C, there is a noticeable shifting of $Cu_2Nb_8O_{21}$ diffraction peaks as well as a continuous decrease in the relative intensity of the (020) reflection, that is, containing the layer of Cu(I) atoms, and that results from the decrease in electron density in this layer. When the $Cu_2Nb_8O_{21}$ particles are heated in air, the products are easily oxidized to give the Cu(II)-containing $CuNb_2O_6$ phase, as well as Nb_2O_5 and $Nb_{12}O_{29}$. These results confirm that $Cu_2Nb_8O_{21}$ is highly unstable toward the loss of the weakly coordinated Cu(I) in the compound. Interestingly, when $Cu_2Nb_8O_{21}$ is kept in the CuCl-flux, no decomposition occurs at temperatures of up to ~650 °C, although at this temperature the Cu(I) ions must be highly mobile.

The formation of Cu(s) at the surfaces by the reduction of Cu(I) must be coupled to a concurrent oxidation reaction. The most likely mechanism which occurs is a Cu(I) disproportionation reaction at the surfaces, that is, $Cu_2Nb_8O_{21} \rightarrow xCu(s) + Cu_{2-x}Nb_8O_{21}$, wherein Cu vacancies as well as oxidized Cu(II) sites form within the $Cu_2Nb_8O_{21}$ structure. This is evidenced in the significant peak shifting and decrease in relative intensity of the (020) reflection described above. This has also previously been observed for other Cu(I) niobates, for example, $CuNbO_3$,[4] as well as for Cu(I) delafossite phases,[30,31] but usually at higher temperatures. The $Cu_2Nb_8O_{21}$ nanoparticles contain much higher amounts of surface water by FT-IR (see Supporting Information, ν(O−H stretch) at ~3300 cm^{-1}) and which explains a more significant extent of disproportionation in this case *versus* the smaller amount of disproportionation for the μm-sized particles. Further, photoelectrochemical data (described below) show an increasing amount of *p*-type dopants, that is, Cu(II) sites, with increasing heating temperatures for polycrystalline films of $Cu_2Nb_8O_{21}$.

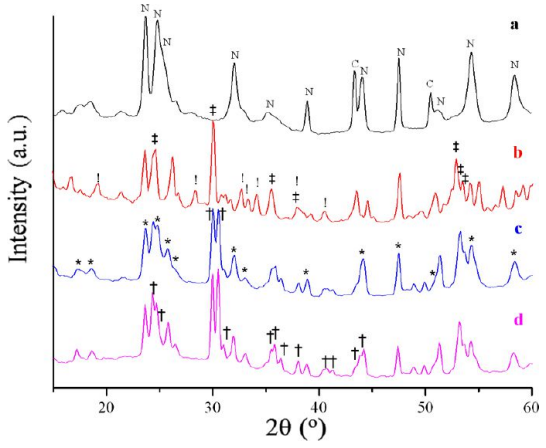

Figure 6. Powder XRD data of the products of heating $Cu_2Nb_8O_{21}$ nanoparticles (a, c) or μm-sized crystals (b, d). These were heated under either N_2 gas to 1000 °C (a, b) or in air up to 900 °C (c, d). Symbols: N = Nb_2O_5, C = Cu, * = $Nb_{12}O_{29}$, † = $CuNb_2O_6$, ‡ = $CuNb_3O_8$, and ! = $CuNbO_3$.

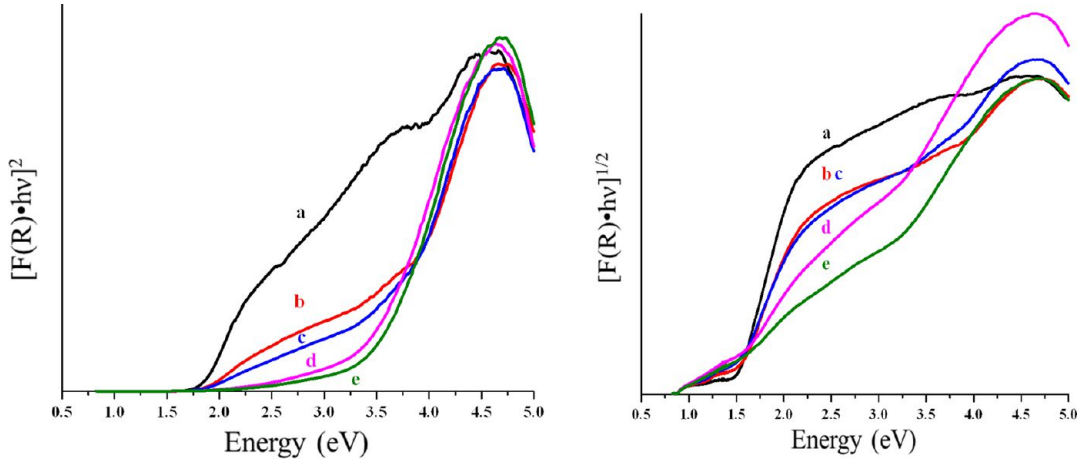

Figure 7. Tauc plots of $[F(R)h\nu]^n$ *vs* $[h\nu]$ for measurement of the direct and indirect band gap sizes, n = 2 (left) and n = 1/2 (right), respectively, of $Cu_2Nb_8O_{21}$ particles. The products were heated to 450 °C for (a) 24 h, (b) 8 h, (c) 5 h, (d) 1 h, and (e) 30 min.

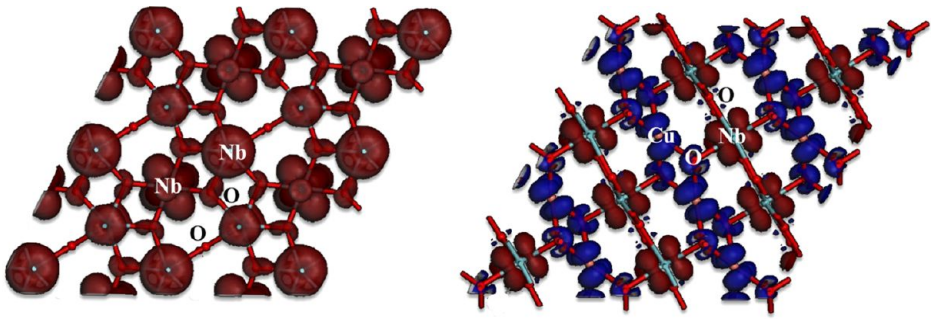

Figure 8. Plots of the electron density in $Cu_2Nb_8O_{21}$ for the uppermost valence band states (blue colored), and lowermost conduction band states (red colored). As in Figure 5, both structural views are perpendicular to the (110) plane, drawn for a single niobate layer (left) and for the neighboring layer comprised of CuO_4 and NbO_7 polyhedra (right). Selected atoms are labeled.

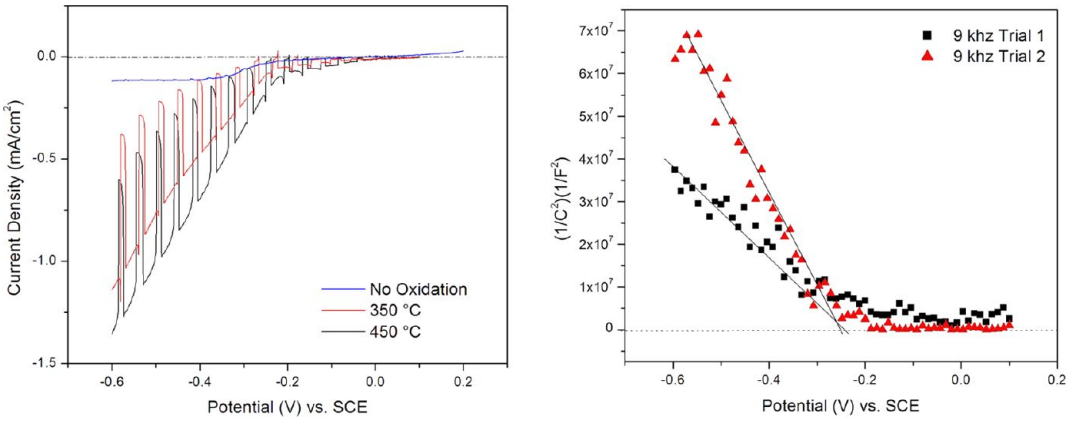

Figure 9. Left, current−potential curves in aqueous 0.5 M Na_2SO_4 solution (pH = 12) under chopped visible-light irradiation for $Cu_2Nb_8O_{21}$ films annealed at 500 °C for 3 h, followed by either no heating in air, or heating in air at 350 or 450 °C for 3 h. Right, plot of Mott−Schottky data for two nonoxidized $Cu_2Nb_8O_{21}$ films.

Optical and Photoelectrochemical Properties. The previously reported Cu(I)-niobates exhibit bandgap sizes within the visible-light energies and have been investigated as efficient *p*-type photoelectrodes for solar energy conversion to hydrogen. Shown in Figure 7 are Tauc plots of UV−vis DRS data for $Cu_2Nb_8O_{21}$ with nano- to μm-sized particles, and listed in Table 1 are the measured bandgap sizes. The lowest energy bandgap transition in all cases is ~1.43 to ~1.65 eV and is indirect and dependent on the particle size. These values compare to the bandgap sizes of $CuNbO_3$ (E_g = 2.0 eV; indirect) and $CuNb_3O_8$ (E_g = 1.26 eV; indirect). The apparent trend of the bandgap size is related to the number of nearest-neighbor Cu−O interactions, where Cu(I) is linearly coordinated in $CuNbO_3$, tetrahedrally coordinated in $Cu_2Nb_8O_{21}$, and octahedrally coordinated in $CuNb_3O_8$. For the higher-energy direct bandgap transition, there is an even more significant blue-shift with decreasing particle size, from ~1.6 eV for the μm-sized crystals to ~3.0 eV for the nanoparticles. Results of electronic structure calculations, Figure 8, show that the lowest-energy bandgap transitions are between filled Cu $3d^{10}$-based crystal orbitals and empty Nb $4d^0$-based crystal orbitals, with a small amount of mixing of the O 2*p* orbitals in each. Thus, a Cu(I)-to-Nb(V) charge transfer occurs as a result of visible-light absorption near the band edges, similar to that found for the other Cu(I)-niobates that function as promising new *p*-type photoelectrodes.[4,5]

The photoelectrochemical properties of polycrystalline $Cu_2Nb_8O_{21}$ photoelectrodes were investigated to confirm the *p*-type nature of this semiconductor. Owing to the highest purity in the μm-sized particles (from the CuCl flux synthesis using Cu_2O nanoparticles at 650 °C), these were used to prepare polycrystalline films that were sintered in a vacuum at ~500 °C and either used as-is or heated in air to 350 or 450 °C for 3 h. The PXRD data confirmed high-purity $Cu_2Nb_8O_{21}$ films. Shown in Figure 9, the polycrystalline films exhibit a strong photocathodic current under visible-light irradiation on the order of ~0.25 to 0.75 mA/cm^2, which is characteristic of a *p*-type semiconductor in the depletion condition. Mott−Schottky measurements also confirm the *p*-type character and locate the energetic positions of the valence and conduction bands at approximately +0.12 to +0.15 V and −1.50 to −1.53 V, respectively, *versus* RHE at a pH = 12. Thus, bandgap excitation of the film causes a charge separation within the depletion region and the migration of the excited

electrons to the surfaces to drive the reduction of water at an overpotential of ~0.8 V. The strongest photocathodic currents are observed for films that are heated in air, where the partial oxidation to Cu(II) occurs (as described above) with increasing temperature and yields increasing *p*-type dopant concentrations. A decrease in the photocurrent and the formation of larger amounts of $CuNb_2O_6$ and Nb_2O_5 side products is found when the films are heated in air to temperatures greater than 500 °C. At 350 and 450 °C, preliminary data show the formation of very small amounts of isolated CuO_x nanoislands on the particle surfaces. These isolated and small islands have recently been found to enhance the charge separation in the Cu(I)-niobate phases, as the photocurrent decreases by about ~10 to ~50% (depending on the specific Cu(I)-niobate phase and its preparation conditions) when they are washed away in acid solutions. The cause of the increasing dark current at the highest bias potentials is currently under investigation. However, a complete investigation of these effects, and of the photoelectrochemical properties of the $Cu_2Nb_8O_{21}$ nanoparticles, is currently in progress and will be reported in a future paper on this topic. These preliminary results can confirm the oxidation of Cu(I) to Cu(II) within the films, and that $Cu_2Nb_8O_{21}$ represents a promising new material for use as a *p*-type photoelectrode that is active for water reduction under visible-light irradiation.

CONCLUSIONS

New, multipored nanoparticles of Li_3NbO_4, ~15−40 nm in diameter, can be synthesized from a hydrothermal reaction using a PEG200/water solution and having a high Li-ion reactivity. These Li_3NbO_4 nanoparticles can be used to prepare new metastable ~4−12 nm particles of $Cu_2Nb_8O_{21}$ from low temperature ion-exchange reactions with CuCl. These nanoparticles grow rapidly within a CuCl flux and yield μm-sized crystals that were characterized by single-crystal X-ray diffraction. The structure consists of a condensed network of NbO_7 polyhedra as well as chains of elongated CuO_4 tetrahedra. The nanoparticles are unstable with respect to the loss of Cu(I) from the structure starting at ~250 °C owing to a disproportionation reaction at its surfaces and, thus, cannot be prepared by conventional solid-state reactions. The bandgap size falls within visible-light energies of ~1.43−1.65 eV, and that electronic structure calculations show originates from the excitation of electrons at the band edges between filled Cu(I) $3d^{10}$-orbitals and empty Nb(V) $3d^0$-orbitals. Polycrystalline films show a strong photocathodic current under visible-light irradiation and Mott−Schottky measurements confirm the *p*-type nature of $Cu_2Nb_8O_{21}$. These results show the general utility of reactive nanoscale precursors in the preparation of new Cu(I)-based semiconducting materials for use in solar energy applications.

METHODS

Synthesis. Nanoparticles of $HNbO_3$ (noncrystalline; <10 nm) were prepared according to a prior literature procedure.[32] Briefly, $NbCl_5$ (Alfa Aesar, 99.9%; 5 g) and dried ethanol (200 proof, 5 mL) were mixed under nitrogen gas. The acidic $Nb(OEt)_5$ ethanol solution was neutralized by addition to a 14.8 M NH_4OH (aq) solution in a 1:5 molar ratio (final pH = 7−8). After stirring the solution for an hour, the solution containing the white powder was centrifuged, decanted, and washed with DI water three times and then washed with ethanol. The white waxy product was dried in an oven at 110 °C for 24 h and then at 200 °C for 12 h, resulting in amorphous $Nb_2O_5 \cdot nH_2O$ (n ~ 3−4; found by TGA) in >95% yield. The product was transferred to a glovebox and ground into a fine powder.

Next, multipored nanoparticles of Li_3NbO_4 were prepared by a hydrothermal reaction of $HNbO_3$ (~1 g), $LiOH \cdot H_2O$ (Alfa Aesar, 99.995%; ~3.2g), distilled water (20 mL), and PEG200 ($C_{2n}H_{4n+2}O_{n+1}$, n = 4; Alfa Aesar; 10 mL) in a 1:5 molar ratio of Nb to Li. These reactants were added to and sealed inside a Teflon-lined stainless-steel reaction vessel and reacted at 180 °C for 24 h (pH ~ 14), following a heating cycle similar to that used for the synthesis of $LiNbO_3$.[18] The basic supernant solution was carefully decanted off and the product was washed with DI water and centrifuged, and this process was repeated for ~7 cycles until the pH reached ~7 to 8, and then washed for a final cycle with ethanol. Note: It is necessary to use high RCF speed of 18700 for 30 min during each cycle in order to reduce the loss of nanoparticles. The powder was dried in an oven at 110 °C for 24 h and then at 200 °C for 3 h, and the powder was immediately transferred to a glovebox. The pale-yellow colored product was identified by powder X-ray diffraction to be >95% yield of high-purity Li_3NbO_4 (ICSD-PDF # 97-010-9053).[33]

Cuprous-niobate nanoparticles were prepared by a solvothermal reaction of the Li_3NbO_4 nanoparticles (0.5 g), PEG200 (20 mL), and CuCl (Alfa Aesar, 99%; 2.78 g) in a 1:10 molar ratio of Nb to Cu, respectively. These reagents were transferred to a 100 mL Teflon liner and stirred for 30 min. Next, the liner was transferred to a sealed stainless steel reaction vessel and heated to 150 °C in a well-insulated sand bath for 5 days with continuous stirring at 300 rpm. The dark orange-colored product was stirred in DI water (150 mL) for 1 h, followed by three cycles of centrifugation and decantation with DI water, and then two washes with ethanol in order to remove all traces of PEG200 and water. This product was then dried in an oven at 110 °C for 24 h. If not used within a few days, it will eventually turn green and fully oxidize over the course of a week or two, yielding $CuNb_2O_6$ (JCPDS # 45-561).[34] This product was loaded into a fused-silica quartz tube, carefully vacuum-dried by a heat-gun up to ~400 °C, and then sealed. Insufficient drying or too much heat treatment can result in oxidization to give CuO and $CuNb_2O_6$. Several parallel reactions were heated from 400 to 450 °C for durations of between 30 min and 24 h. Each time the products were washed with NH_4OH (14.8 M) to remove the remaining excess CuCl and Cu_2O. High-purity nanosized and μm-sized crystals of $Cu_2Nb_8O_{21}$ are obtained in about >90% yield, depending on the heating duration (Note: Excessive washing of the $Cu_2Nb_8O_{21}$ nanoparticles in *c*-NH_4OH causes significant Cu(I) loss for more than five washing cycles for 1 g of product mixture). Larger single crystals were also obtained for structural characterization by single crystal X-ray diffraction by a reaction at 650 °C for 24 h.

Characterization. All products were characterized by powder X-ray diffraction (PXRD) at room temperature on a Rigaku R-Axis Spider with a curved image plate detector and Cu Kα1 (λ = 1.54056 Å) radiation from a sealed-tube X-ray source (40 kV, 36 mA). A single-crystal X-ray analysis was performed

on a Bruker-Nonius X8 Apex2 diffractometer at a temperature of 223 K. The frame integration was performed using the SAINT program.[35] The resulting raw data were scaled and absorption corrected using a multiscan averaging of symmetry equivalent data using SADABS.[36] Each structure was solved by direct methods and refined by full-matrix least-squares fitting on F^2 using SHELXTL-97.[37] Selected data collection and refinement parameters are listed in Table S1, and interatomic distances and angles are found in Table S2. Included in the Supporting Information is a complete list of data collection and refined structural and atomic parameters.

Thermogravimetric analyses were performed using a DSC-TGA (TA Instruments TGA Q50 and SDT 2960 systems) on the nanosized and μm-sized crystallites of $Cu_2Nb_8O_{21}$, as well as on the $HNbO_3$ and Li_3NbO_4 reactants. Weighed amounts (~20 mg) of each were loaded onto a Pt pan, equilibrated at room temperature, and then heated under either air or flowing N_2 up to 200 to 1000 °C at a rate of 5 °C/min. Post-TGA residuals were characterized by powder X-ray diffraction in transmission mode on a Rigaku R-Axis Spider system as described above. Specific surface area measurements were performed on dried products (200 °C for 3 h) on a ChemBET Pulsar TPR/TPD instrument. For each sample, FT-IR data were collected on Shimadzu IR-prestige 21 spectrophotometer equipped with sample stage and a GladiATR accessory (PIKE Technology). The UV−vis diffuse reflectance spectra (DRS) for samples were collected on a Shimadzu UV-3600 spectrophotometer equipped with an integrating sphere. Approximately 20 mg of each sample was mounted onto a sample holder by pressing the powder into a $BaSO_4$ matrix and placing it along the external window of the integrating sphere. A sample of pure pressed barium sulfate powder was prepared as a reference, and the data were plotted as the function $F(R) = (1 - R_\infty)^2/(2R_\infty)$, where R is diffuse reflectance based on the Kubelka−Munk theory of diffuse reflectance.[38,39] Because $F(R)$ is also equal to k/s, where k and s are the absorption and scattering coefficients, the bandgap sizes can be extracted *via* Tauc plots of $[F(R)h\nu]^n$ *versus* $h\nu$, where $n = 1/2$ and 2 for indirect and direct bandgap sizes, respectively.

Scanning electron microscopy of the samples were performed on a JEOL SEM 6400 field-emission scanning electron microscope (FESEM) at 10.0 kV, and the energy dispersive X-ray (EDX) data were collected on 4Pi Isis EDS system at Hitachi S3200 at 20.0 kV, variable pressure scanning electron microscope as a check of the elemental compositions. Transmission electron microscopy (TEM) images and selected area electron diffraction (SAED) were acquired on an FEI Tecnai G^2 twin microscope operated at an accelerating voltage of 200 keV and equipped with a TIA digital camera. Sample preparation consisted of drop casting 1 mg/mL sample solutions onto a carbon-Formvar 200 mesh copper grid (EMS).

Photoelectrochemical Measurements. Polycrystalline films were prepared on fluorine-doped tin oxide (FTO) glass slides (TEC-15 from Pilkington Glass Inc.). The FTO glass slides were cleaned by sonication in deionized water, acetone, and ethanol for 30−45 min. A 2 × 2 cm^2 area was masked off the FTO slides using Scotch tape, the powders were ground in ethanol as a dispersant and deposited as a film using the drop cast technique. All films were annealed under vacuum at 500 °C, and the films were either not heated further or were heated in air at 350 or 450 °C for 3 h. All electrochemical experiments were carried out in a Teflon cell using a three-electrode system, with the polycrystalline film as the working electrode, Pt as the counter-electrode, and a standard calomel reference electrode (satd KCl). Argon gas was bubbled through the electrolyte solution (0.5 M Na_2SO_4) for 30 min before the measurements; the pH of the solution was adjusted using NaOH(aq). All polycrystalline films were irradiated from the backside using a 400 W Xe arc-lamp equipped with visible-light cutoff and bandpass filter ($\lambda \geq 420$ nm). Cyclic voltammetric measurements were carried out under chopped visible light irradiation with an applied bias voltage range of 200 to −600 mV *vs* SCE.

Electronic Structure Calculations. Band-structure calculations were performed for the geometry-optimized structure of $Cu_2Nb_8O_{21}$ with the use of the plane-wave density functional theory package CASTEP.[40] The Perdew−Burke−Ernzerhof functional in the generalized gradient approximation and ultrasoft core potentials were employed in the calculations.[41] The selection of equally distributed k-points within the Brillouin zone was automatically calculated according to the Monkhorst−Pack scheme.[42]

Conflict of Interest: The authors declare no competing financial interest.

Acknowledgment. The authors acknowledge financial support from the Research Corporation for Science Advancement (P.M. is a Scialog awardee) and from the National Science Foundation (DMR-0644833), and assistance from P. Boyle for collection of the single crystal X-ray data set and the structure refinement, C. Mooney for SEM images and EDS data, J. Stecher for TEM images and ED measurements, C. Melander for use of a high-speed centrifuge, and J. Martin for use of a TGA-DSC.

Supporting Information Available: The crystallographic information file for $Cu_2Nb_8O_{21}$, tables of interatomic distances and selected single-crystal refinement data, powder X-ray diffraction data for the decomposition, and washing of Li_3NbO_4 for the decomposition of $Cu_2Nb_8O_{21}$ in air or N_2(g), for both before and after the annealing, oxidation, and photoelectrochemical measurements, a description of the Mott−Schottky measurements and calculations, histograms of particle sizes, and FT-IR data and SEM/TEM images on all of the $Cu_2Nb_8O_{21}$ products. This material is available free of charge *via* the Internet at http://pubs.acs.org.

REFERENCES AND NOTES

1. Osterloh, F. E. Inorganic Materials as Catalysts for Photochemical Splitting of Water. *Chem. Mater.* **2008**, *20*, 35–54.
2. Kudo, A.; Miseki, Y. Heterogeneous Photocatalyst Materials for Water Splitting. *Chem. Soc. Rev.* **2009**, *38*, 253–278.
3. Joshi, U. A.; Maggard, P. A. Semiconducting Oxides to Facilitate the Conversion of Solar Energy to Chemical Fuels. *J. Phys. Chem. Lett.* **2010**, *1*, 2719–2726.
4. Joshi, U.; Palasyuk, A.; Maggard, P. A. Photoelectrochemical Investigation and Electronic Structure of a p-Type $CuNbO_3$ Photocathode. *J. Phys. Chem. C* **2011**, *115*, 13534–13539.
5. Joshi, U.; Maggard, P. A. $CuNb_3O_8$: A p-Type Semiconducting Metal Oxide Photoelectrode. *J. Phys. Chem. Lett.* **2012**, *3*, 1577–1581.
6. Fuoco, L.; Joshi, U. A.; Maggard, P. A. Preparation and Photoelectrochemical Properties of p-Type $Cu_5Ta_{11}O_{30}$ and $Cu_3Ta_7O_{19}$ Semiconducting Polycrystalline Films. *J. Phys. Chem. C* **2012**, *116*, 10490–10497.
7. Palasyuk, O.; Palasyuk, A.; Maggard, P. A. Site-Differentiated Solid Solution in $(Na_{1-x}Cu_x)_2Ta_4O_{11}$ and Its Electronic Structure and Optical Properties. *J. Solid State Chem.* **2010**, *183*, 814–822.
8. *Nanostructured and Photoelectrochemical Systems for Solar Photon Conversion*; Archer, M. D., Nozik, A. J., Eds.; Imperial College Press: London, U.K., 2008.
9. Kay, A.; Cesar, I.; Grätzel, M. New Benchmark for Water Photooxidation by Nanostructured α-Fe_2O_3 Films. *J. Am. Chem. Soc.* **2006**, *128*, 15714–15721.
10. Townsend, T. K.; Browning, N. D.; Osterloh, F. E. Nanoscale Strontium Titanate Photocatalysts for Overall Water Splitting. *ACS Nano* **2012**, *6*, 7420–7426.
11. Sabio, E. M.; Chamousis, R. L.; Browning, N. D.; Osterloh, F. E. Photocatalytic Water Splitting with Suspended Calcium Niobium Oxides: Why Nanoscale is Better than the Bulk, A Kinetic Analysis. *J. Phys. Chem. C* **2012**, *116*, 3161–3170.
12. Arney, D.; Watkins, T.; Maggard, P. A. Effect of Particle Surface Areas and Microstructures on Photocatalytic H_2 and O_2 Production over $PbTiO_3$. *J. Am. Ceram. Soc.* **2011**, *94*, 1483–1489.
13. Arney, D.; Hardy, C.; Greve, B.; Maggard, P. A. Flux Synthesis of $AgNbO_3$: Effect of Particle Surfaces and Sizes on Photocatalytic Activity. *J. Photochem. Photobiol., A* **2010**, *214*, 54–60.
14. Kamat, P. V.; Tvrdy, K.; Baker, D. R.; Radich, J. G. Beyond Photovoltaics: Semiconductor Nanoarchitectures for Liquid-Junction Solar Cells. *Chem. Rev.* **2010**, *110*, 6664–6688.

15. Zhang, J.; Bang, J. H.; Tang, C.; Kamat, P. V. Tailored TiO_2–$SrTiO_3$ Heterostructure Nanotube Arrays for Improved Photoelectrochemical Performance. *ACS Nano* **2010**, *4*, 387–395.
16. Joshi, U.; Jang, J.; Borse, P.; Lee, J. Microwave Synthesis of Single-Crystalline Perovskite $BiFeO_3$ Nanocubes for Photoelectrode and Photocatalytic Applications. *Appl. Phys. Lett.* **2008**, *92*, 242106–242110.
17. Modeshia, D. R.; Walton, R. I. Solvothermal Synthesis of Perovskites and Pyrochlores: Crystallisation of Functional Oxides Under Mild Conditions. *Chem. Soc. Rev.* **2010**, *39*, 4303–4325.
18. Modeshia, D. R.; Walton, R. I.; Mitchell, M. R.; Ashbrook, S. E. Disordered Lithium Niobate Rock-Salt Materials Prepared by Hydrothermal Synthesis. *Dalton Trans.* **2010**, *39*, 6031–6036.
19. Huang, J.; Chen, Z.; Zhang, Z.; Zhu, C.; He, H.; Ye, Z.; Qu, G.; Tong, L. Synthesis and Waveguiding of Single-Crystalline $LiNbO_3$ Nanorods. *Appl. Phys. Lett.* **2011**, *98*, 093102–1 – 093102–3.
20. Nyman, M.; Anderson, T. M.; Provencio, P. P. Comparison of Aqueous and Non-Aqueous Soft-Chemical Syntheses of Lithium Niobate and Lithium Tantalate Powders. *Cryst. Growth Des.* **2009**, *9*, 1036–1040.
21. Reddy Channu, V. S.; Holze, R.; Walker, E. H., Jr.; Wicker, S. A., Sr.; Kalluru, R. R.; Williams, Q. L.; Walters, W. Synthesis and Characterization of Lithium Vanadates for Electrochemical Applications. *Int. J. Electrochem. Sci.* **2010**, *5*, 1355–1366.
22. Sebastian, L.; Gopalakrishnan, J. Lithium Ion Mobility in Metal Oxides: A Materials Chemistry Perspective. *J. Mater. Chem.* **2003**, *13*, 433–441.
23. Luo, C.; Xue, D. Mild, Quasireverse Emulsion Route to Submicrometer Lithium Niobate Hollow Spheres. *Langmuir* **2006**, *22*, 9914–9918.
24. Hsiao, Y.-J.; Fang, T.-H.; Lin, S.-J.; Shieh, J.-M.; Ji, L.-W. Preparation and Luminescent Characteristic of Li_3NbO_4 Nanophosphor. *J. Lumin.* **2010**, *130*, 1863–1865.
25. Marinder, B.-O.; Wahlström, E. $CuNbO_3$, A Structure with Stepped NbO_3 Layers. *Chem. Scr.* **1984**, *23*, 157–160.
26. Marinder, B.-O.; Werner, P.-E.; Wahlström, E.; Malmros, G. Investigations on New Copper Niobium Oxide of $LiNb_3O_8$ Type Using Chemical Analysis and X-ray Powder Diffraction Profile Analysis. *Acta Chem. Scand. A* **1980**, *34*, 51–56.
27. Palasyuk, O.; Maggard, P. A. $NaCu(Ta_{1-y}Nb_y)_4O_{11}$ Solid Solution: A Tunable Band Gap Spanning the Visible-Light Wavelengths. *J. Solid State Chem.* **2012**, *191*, 263–270.
28. Hormillosa, C. *Bond Valence Calculator* (v. 2.0), 1993.
29. Altermatt, D.; Brown, I. D. Bond-Valence Parameters Obtained From a Systematic Analysis of the Inorganic Crystal Structure Database. *Acta Crystallogr., Sect. B: Struct. Sci.* **1985**, *41*, 244–247.
30. Hamada, I.; Katayama-Yoshida, H. Energetics of Native Defects in $CuAlO_2$. *Phys. B (Amsterdam, Neth.)* **2006**, *376–377*, 808–811.
31. Garlea, O.; Darie, C.; Bougerol, C.; Isnard, O.; Bordet, P. Structure of $LaCuO_{2.66}$: An Oxidized Delafossite Compound Containing Hole-Doped Kagome Planes of Cu^{2+} Cations. *Solid State Sci.* **2003**, *5*, 1095–1104.
32. Uekawa, N.; Kudo, A.; Mori, F.; Wu, Y. J.; Kakegawa, K. Low-Temperature Synthesis of Niobium Oxide Nanoparticles from Peroxo Niobic Acid Sol. *J. Colloid Interface Sci.* **2003**, *264*, 378.
33. Weis, R. S.; Gaylord, T. K. Lithium Niobate: Summary of Physical Properties and Crystal Structure. *Appl. Phys. A: Mater. Sci. Process.* **1985**, *37*, 191.
34. Drew, M. G. B.; Hobson, R. J.; Padayatchy, V. T. Synthesis, Structure and Magnetic Properties of Monoclinic $CuNb_2O_6$ and the Electronic Spectra of Both Polymorphs of $CuNb_2O_6$. *J. Mater. Chem.* **1995**, *5*, 1779–1783.
35. Bruker-Nonius, *SAINT+*, version 7.07B, Bruker-Nonius, Madison, WI 53711, U.S.A., 2004.
36. Bruker-Nonius, *SADABS*, version 2.10, Bruker-Nonius, Madison, WI 53711, U.S.A., 2004
37. Sheldrick, G. M. *SHELXTL NT*, Software Package for Refinement of Crystal Structures, ver. 5.10; Bruker Analytical X-ray Instruments, Inc.: Madison,WI, 1998.
38. Kortum, G. *Reflectance Spectroscopy*; Springer-Verlag: New York, NY, 1969.
39. Weckhuysen, B. M.; Schoonhedt, R. A. Recent Progress in Diffuse Reflectance Spectroscopy. *Catal. Today* **1999**, *49*, 441–451.
40. Clark, S. J.; Segall, M. D.; Pickard, C. J.; Hasnip, P. J.; Probert, M. J.; Refson, K.; Payne, M. C. First Principle Methods Using CASTEP. *Z. Kristallogr.* **2005**, *220*, 567.
41. Payne, M. C.; Teter, M. P.; Allan, D. C.; Arias, T. A.; Joannopoulos, J. D. Iterative Minimization Techniques for *Ab Initio* Total-Energy Calculations: Molecular Dynamics and Conjugate Gradients. *Rev. Mod. Phys.* **1992**, *64*, 1045.
42. Monkhorst, H. J.; Pack, J. D. Special Points for Brillouin-Zone Integrations. *Phys. Rev. B* **1976**, *13*, 5188.